INTERNATIONAL JOURNAL FOR NUMERICAL METHODS IN FLUIDS
Int. J. Numer. Meth. Fluids 2006; **51**:1319–1334
Published online 4 January 2006 in Wiley InterScience (www.interscience.wiley.com). DOI: 10.1002/fld.1157

Reynolds stress modelling of rectangular open-channel flow

Hyeongsik Kang[‡] and Sung-Uk Choi[*,†]

School of Civil and Environmental Engineering, Yonsei University, Seoul, South Korea

SUMMARY

A Reynolds stress model for the numerical simulation of uniform 3D turbulent open-channel flows is described. The finite volume method is used for the numerical solution of the flow equations and transport equations of the Reynolds stress components. The overall solution strategy is the SIMPLER algorithm, and the power-law scheme is used to discretize the convection and diffusion terms in the governing equations. The developed model is applied to a flow at a Reynolds number of 77 000 in a rectangular channel with a width to depth ratio of 2. The simulated mean flow and turbulence structures are compared with measured and computed data from the literature. The computed flow vectors in the plane normal to the streamwise direction show a small vortex, called inner secondary currents, located at the juncture of the sidewall and the free surface as well as the free surface and bottom vortices. This small vortex causes a significant increase in the wall shear stress in the vicinity of the free surface. A budget analysis of the streamwise vorticity is carried out. It is found that both production terms by anisotropy of Reynolds normal stress and by Reynolds shear stress contribute to the generation of secondary currents. Copyright © 2006 John Wiley & Sons, Ltd.

KEY WORDS: open-channel flows; turbulence; Reynolds stress model; secondary currents; inner secondary currents; budget analysis

INTRODUCTION

Open-channel flows are characterized by complicated flow structures, even for simple geometry, such as that of a rectangular channel. This is largely due to wall and free surface boundaries. They play an important role in the distribution of turbulent energy. Walls and free surface reduce the turbulence intensity in the direction normal to the surface, and the decreased turbulence intensity is redistributed in the other two directions. The anisotropy of

*Correspondence to: Sung-Uk Choi, School of Civil and Environmental Engineering, Yonsei University, Seoul, South Korea.
†E-mail: schoi@yonsei.ac.kr
‡E-mail: kanghs@yonsei.ac.kr

Contract/grant sponsor: MOCT KOREA; contract/grant number: 03-SANHAKYOUN-C03-01

Received 25 May 2005
Revised 4 November 2005
Accepted 7 November 2005

turbulence, which is strengthened by wall and free surface boundaries, is known to generate secondary currents in open-channel flows.

Secondary currents observed in a straight open-channel are classified as secondary currents of Prandtl's second kind. Although the magnitude of the secondary currents is only about 2% of the maximum streamwise velocity [1], they have a major effect on the mean flow and turbulence structures. Due to the secondary currents, the location of the maximum streamwise velocity occurs below the water surface [2], and the velocity contour lines are bulged towards the corners [3]. Secondary currents also increase bed shear stress near the corner [4], which may affect the sediment transport capacity of the open-channel significantly.

Previous studies have revealed that secondary motions in the cross section of open-channel flows consist of two large vortices, namely a free surface vortex and a bottom vortex [1, 5]. However, recently, Grega *et al.* [6] and Hsu *et al.* [7] reported on the existence of inner secondary currents at the juncture of the free surface and sidewall in the rectangular channel. The small-sized vortex, as seen in Figure 1, affects the mean flow and turbulence structure, thus significantly affecting the shear stress distribution at the wall in the region close to the free surface.

For numerical simulations of 3D turbulent open-channel flows, as in other engineering problems, the k–ε model has been the preferred choice in hydraulics [8–14]. However, since the standard k–ε model is an isotropic turbulence closure based on the eddy viscosity concept, it cannot reproduce directional effects of turbulent flows such as secondary motions of fluids in the plane normal to the streamwise direction [15, 16].

In general, there are three principal approaches for improving turbulence models based on the eddy viscosity concept [17]. One is to generalize the linear stress rate of the strain law by including a nonlinear effect. An example of this is the nonlinear k–ε model, an anisotropic turbulence closure. This model has been employed to predict open-channel flows with secondary currents [15, 18, 19]. Although their modelling was successful in simulating secondary currents in a compound channel, especially at the juncture of the main channel and

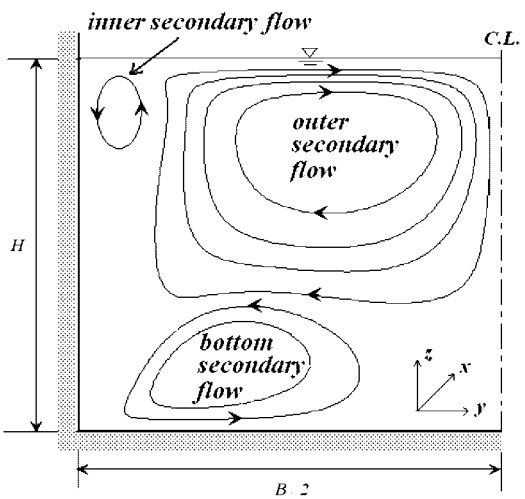

Figure 1. Schematic view of secondary flows in rectangular open-channel.

floodplain, details of the mean flow and turbulence structure were not accurately simulated by the nonlinear k–ε model. For example, the velocity-dip phenomenon can hardly be found in the computed velocity profiles.

The second approach is to use algebraic relationships for Reynolds stresses (Algebraic Stress Model: ASM). The ASM is economical because it solves algebraic relationships that have been derived or simplified from the Reynolds stress transport equations. Previously, Naot and Rodi [5] proposed an ASM to numerically simulate open-channel flows with secondary currents. Following this, many researchers simulated open-channel flows using the ASM [20–22]. However, since the ASM does not solve the exact equations for Reynolds stresses, but solves empirical relationships for computational stability instead [23], the simulated mean flow and turbulence structures are not sufficiently accurate.

Finally, the third approach is to determine the Reynolds stress by solving the Reynolds stress transport equations directly (Reynolds Stress Model: RSM). Unlike the ASM, in the RSM, it is not necessary to introduce *ad hoc* expressions for the Reynolds stress. However, due to the complexity of the model, the application of the RSM to open-channel flows is limited. Reece [24] is the first investigator who developed the RSM based on Launder *et al.*'s [25] model, and he simulated both square duct flow and open-channel flow. Later, Cokljat and Younis [16, 26] and Basara and Cokljat [27] proposed the RSM for numerical simulations of free surface flows in a rectangular channel and in a compound channel and found good agreement between predicted and measured data. However, no previous studies have appeared on the RSM applied to open-channel flows that focus on the detailed mean flow and turbulence structure including inner secondary currents.

The purpose of the present study was to develop a RSM for the numerical simulation of rectangular open-channel flows. The proposed RSM consists of Speziale *et al.*'s [28] model for the pressure–strain term, Mellor and Herring's [29] model for the diffusion term, and Rotta's [30] model for the dissipation term. Using the developed model, the mean flow and turbulence structures were simulated and the results obtained were compared with existing numerical and experimental data. The model was verified to reproduce secondary currents including inner and outer free surface vortices and bottom vortex properly. A budget analysis of the streamwise vorticity equation was also performed to investigate the mechanism by which these secondary currents are generated.

MATHEMATICAL MODEL

Consider steady open-channel flow at a high Reynolds number, and assume that the flow is uniform in the streamwise direction. If we denote the mean and turbulent velocities by $\overline{u_i}$ and u_i' in the i-direction, respectively, then the continuity and momentum equations are given by

$$\frac{\partial \bar{v}}{\partial y} + \frac{\partial \bar{w}}{\partial z} = 0 \tag{1}$$

$$\bar{v}\frac{\partial \bar{u}}{\partial y} + \bar{w}\frac{\partial \bar{u}}{\partial z} = \frac{\partial}{\partial y}\left(\nu\frac{\partial \bar{u}}{\partial y} - \overline{u'v'}\right) + \frac{\partial}{\partial z}\left(\nu\frac{\partial \bar{u}}{\partial z} - \overline{u'w'}\right) + gS_o \tag{2}$$

$$\bar{v}\frac{\partial \bar{v}}{\partial y} + \bar{w}\frac{\partial \bar{v}}{\partial z} = -\frac{1}{\rho}\frac{\partial \bar{p}}{\partial y} + \frac{\partial}{\partial y}\left(\nu\frac{\partial \bar{v}}{\partial y} - \overline{v'^2}\right) + \frac{\partial}{\partial z}\left(\nu\frac{\partial \bar{v}}{\partial z} - \overline{v'w'}\right) \tag{3}$$

$$\bar{v}\frac{\partial \bar{w}}{\partial y} + \bar{w}\frac{\partial \bar{w}}{\partial z} = -\frac{1}{\rho}\frac{\partial \bar{p}}{\partial z} + \frac{\partial}{\partial y}\left(\nu\frac{\partial \bar{w}}{\partial y} - \overline{v'w'}\right) + \frac{\partial}{\partial z}\left(\nu\frac{\partial \bar{w}}{\partial z} - \overline{w'^2}\right) \tag{4}$$

where x, y, and z are the streamwise, transverse, and vertical directions, $\bar{u}$ the streamwise mean velocity, $\bar{v}$ and $\bar{w}$ the components of the secondary motion as sketched in Figure 1, $\bar{p}$ the mean pressure, ν the kinematic viscosity, $-\overline{u_i'u_j'}$ the Reynolds stress, g the gravitational acceleration, and S_o the channel slope.

The Reynolds stress in the momentum equations is obtained by solving the transport equations for Reynolds stress R_{ij} $(=\overline{u_i'u_j'})$ such as

$$\overline{u_k}\frac{\partial R_{ij}}{\partial x_k} = -\left(R_{ik}\frac{\partial \overline{u_j}}{\partial x_k} + R_{jk}\frac{\partial \overline{u_i}}{\partial x_k}\right) + D_{ij} - \varepsilon_{ij} + \Pi_{ij} \tag{5}$$

where D_{ij} is the transport of R_{ij} by diffusion, ε_{ij} the rate of dissipation of R_{ij}, and Π_{ij} the transport of R_{ij} due to turbulent pressure–strain interactions. Choi and Kang [31] carried out numerical experiments of various RSMs in computing the vertical structure of an open-channel flow by comparing three diffusion models and five pressure–strain models. They found that the diffusion model of Mellor and Herring [29] and the pressure–strain model of Speziale *et al.* [28] reproduce the measured data best. These models are used herein. Choi and Kang's [31] result conforms to the findings from an earlier study by Demuren and Sarkar [32], who tested three diffusion models and five pressure strain models in computing channel flows without free surface.

For D_{ij}, the following model proposed by Mellor and Herring [29] is used:

$$D_{ij} = C_s\frac{\partial}{\partial x_k}\left[\frac{k^2}{\varepsilon}\left(\frac{\partial R_{ij}}{\partial x_k} + \frac{\partial R_{ik}}{\partial x_j} + \frac{\partial R_{jk}}{\partial x_i}\right)\right] \tag{6}$$

where C_s is a model constant $(=0.22/3)$ and k is the turbulent kinetic energy $(=R_{ii}/2)$. In the present study, for the dissipation rate of R_{ij}, the following model by Rotta [30] is used:

$$\varepsilon_{ij} = \tfrac{2}{3}\varepsilon\delta_{ij} \tag{7}$$

in which ε is the dissipation rate of k and δ_{ij} the Kronecker's delta. The dissipation rate of k is obtained by solving the standard transport equation such as

$$\overline{u_j}\frac{\partial \varepsilon}{\partial x_j} = \frac{\partial}{\partial x_k}\left(C_\varepsilon\frac{k}{\varepsilon}R_{kl}\frac{\partial \varepsilon}{\partial x_l}\right) + \frac{\varepsilon}{k}(C_{\varepsilon 1}P_k - C_{\varepsilon 2}\varepsilon) \tag{8}$$

where P_k is the rate of production of turbulence kinetic energy and C_ε $(=0.18)$, $C_{\varepsilon 1}$ $(=1.45)$, and $C_{\varepsilon 2}$ $(=1.90)$ are empirical constants.

The last term in Equation (5) is the pressure–strain term which acts to redistribute turbulent kinetic energy among the Reynolds stresses. The present RSM employs the following model proposed by Speziale *et al.* [28] for Π_{ij} in Equation (5), named SSG model hereafter

$$\begin{aligned}\Pi_{ij} = {} & \alpha_0\varepsilon b_{ij} + \alpha_1\varepsilon(b_{ik}b_{jk} - 1/3\cdot b_{mn}b_{nm}\delta_{ij}) + \alpha_2 kS_{ij} + \alpha_3 P_k b_{ij} \\ & + \alpha_4 k(b_{ik}S_{jk} + b_{jk}S_{ik} - 2/3\cdot b_{kl}S_{kl}\delta_{ij}) + \alpha_5 k(b_{ik}W_{jk} + b_{jk}W_{ik})\end{aligned} \tag{9}$$

where b_{ij} is the anisotropy tensor, S_{ij} the rate of the strain tensor, W_{ij} the rotation tensor, and α_0–α_5 empirical coefficients. The values of these parameters used herein are from Speziale *et al.* [28], i.e. $\alpha_0 = -3.4$, $\alpha_1 = 4.2$, $\alpha_2 = 0.8 - 1.3\ (b_{mn}b_{nm})^{1/2}$, $\alpha_3 = -1.8$, $\alpha_4 = 1.25$, and $\alpha_5 = 0.4$. In Equation (9), b_{ij}, S_{ij}, and W_{ij} are given, respectively, by

$$b_{ij} = \frac{R_{ij}}{2k} - \frac{1}{3}\delta_{ij} \tag{10a}$$

$$S_{ij} = \frac{1}{2}\left(\frac{\partial \overline{u_i}}{\partial x_j} + \frac{\partial \overline{u_j}}{\partial x_i}\right) \tag{10b}$$

$$W_{ij} = \frac{1}{2}\left(\frac{\partial \overline{u_i}}{\partial x_j} - \frac{\partial \overline{u_j}}{\partial x_i}\right) \tag{10c}$$

In the right-hand side of Equation (9), the first term is the usual Rotta term for the return to isotropy, which is included in most Reynolds stress models. The second term is a nonlinear contribution to the return to isotropy. Both terms represent the slow contribution to the pressure–strain correlation, while the remaining four terms represent rapid contributions. The third term is linear and the fourth is quadratic in b_{ij}. The fifth and the last terms are also linear in b_{ij}, and these two terms are known to make a major contribution in the rapid portion.

The damping effects of the wall and the free surface are very similar, and act to increase the level of anisotropy. However, in the vicinity of the free surface, the mean velocity gradients are negligible. This is the reason why the SSG model used here was found not to be very suitable near the free surface [27]. Therefore, in order to consider the damping effects at the free surface, the following combinations of Shir [33] and Gibson and Launder [34] models are added to the pressure–strain term:

$$\begin{aligned}\Pi_{ij,f_s} = {} & C_{f_s,1}\frac{\varepsilon}{k}\left(R_{km}n_k n_m\delta_{ij} - \frac{3}{2}R_{ki}n_k n_j - \frac{3}{2}R_{kj}n_k n_i\right)\cdot f_s \\ & + C_{f_s,2}\left(\Pi_{km,2}n_k n_m\delta_{ij} - \frac{3}{2}\Pi_{ki,2}n_k n_j - \frac{3}{2}\Pi_{kj,2}n_k n_i\right)\cdot f_s\end{aligned} \tag{11}$$

where $C_{f_s,1}$ $(=0.5)$ and $C_{f_s,2}$ $(=0.1)$ are model constants and f_s the free surface damping function given by

$$f_s = \left(\frac{L}{z_n^{-1} + C_f L}\right)^2 \tag{12}$$

where L is the turbulence length scale $(= C_\mu^{3/4}k^{1.5}/(\kappa\varepsilon))$, z_n the vertical distance from the free surface, and C_f $(=0.16)$ an empirical constant. Model constants $C_{f_s,1}$ and $C_{f_s,2}$, were given by Shir [33] and Gibson and Launder [34], respectively, and C_f was calibrated by Cokljat [35] for free surface flows.

In the present study, the finite volume method is used to solve the flow equations and the transport equations of the Reynolds stress components. Since the flow is assumed to be fully developed and uniform in the streamwise direction, the spatial derivatives with respect

to the streamwise direction are ignored in the flow equations. This reduces the flow equations parabolic in the streamwise direction and elliptic in the transverse direction. For the solution strategy, the SIMPLER algorithm proposed by Patankar and Spalding [36] is employed. The SIMPLER algorithm, a revised SIMPLE algorithm, is used to obtain the cross stream pressure field. For the discretizations of the convection term and diffusion term in the governing equations, the power-law differencing scheme by Patankar [37] is used. A detailed computational procedure is described in Reference [38].

Boundary conditions are required at the walls and at the free surface. It is assumed that the flow at the node closest to the wall obeys the standard logarithmic law. Since local equilibrium is assumed in the vicinity of the wall, the dissipation rate is set equal to the production of the turbulence kinetic energy. For the Reynolds normal stress at the wall, the zero gradient condition is used. The Reynolds shear stress at the wall vicinity is set equal to the value from the logarithmic law. The free surface is treated as a symmetric plane for all dependent variables except for the dissipation rate of the turbulent kinetic energy (ε). For ε, the relationship by Naot and Rodi [5] is prescribed at the free surface in order to increase the dissipation level of turbulence kinetic energy.

MEAN FLOW AND TURBULENCE STRUCTURES

Using the developed RSM, an open-channel flow was simulated. A water depth of 0.1 m, a channel width of 0.2 m, and a slope of 0.00059 yield a streamwise mean velocity of 0.387, a maximum streamwise velocity of 0.46 m/s, and a shear velocity of 0.014 m/s at the bottom. The Reynolds number based on the streamwise mean velocity and hydraulic radius is 77 000. The numbers of grid points used in the present study are 100 and 120 in the y- and z-directions, respectively. The results, simulated by the RSM, are compared not only with experimental measurements by Nezu and Rodi [1] but also with another RSM data by Cokljat [35] and LES data by Shi *et al.* [39]. The RSM by Cokljat [35] is composed of Launder *et al.*'s [25] model for the pressure–strain correlation term, Daly and Harlow's [40] model for the diffusion of R_{ij}, and Rotta's [30] model for the dissipation of R_{ij}. The experimental or simulated data used for comparisons are from flows at relatively high Reynolds numbers ranging from 73 000 to 97 000. Thus, these values of the Reynolds numbers are comparable to that of the present simulations.

Figure 2 shows the contours of the streamwise mean velocity normalized by its maximum value. It can be seen that the streamwise mean velocity predicted by the present RSM is in good agreement with the measured profiles and with the other simulated data. Note that the velocity contour lines predicted by the RSM are bulged towards the juncture between the sidewall and free surface, which is not seen in the other profiles in the figure. This is caused by inner secondary currents in the vicinity of the juncture, which are discussed below.

Secondary current vectors are given in Figures 3(a)–(d). In all figures, the free surface vortex and the bottom vortex are observed. Specifically, the overall pattern and the magnitudes of the secondary currents predicted by the present RSM are seen to coincide with measured and other numerical results. In Figure 3(a), the computed maximum magnitude of the secondary current vectors appears to be about 2% of the maximum value of the streamwise mean velocity, which is consistent with previous findings, i.e. Naot and Rodi [5], Tominaga *et al.* [41], and Cokljat and Younis [16]. Only in the velocity vectors predicted by the present

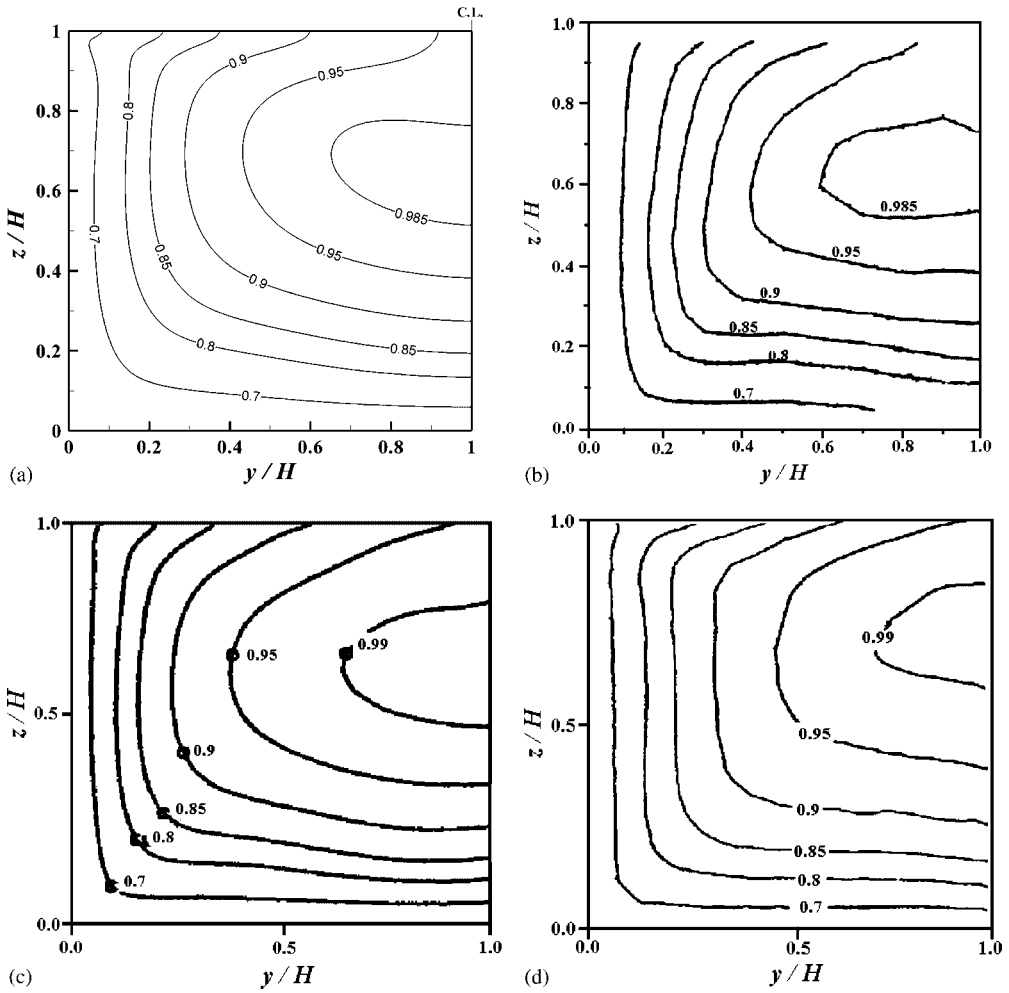

Figure 2. Streamwise velocity contours ($\bar{u}/\bar{u}_{\max}$): (a) present RSM; (b) experiment [1]; (c) RSM [35]; and (d) LES [39].

RSM, namely in Figure 3(a), a small vortex is observed at the juncture between the free surface and the sidewall. Grega *et al.* [6] referred to this small vortex as the inner secondary vortex and to the large vortex as the outer secondary vortex. Despite the low intensity of the inner secondary vortex, whose magnitude is known to be about 1% of the mean value of the streamwise velocity [6], it is expected that the inner secondary currents affect the distribution of the shear stress at the sidewall [42]. This small vortex, however, is not observed in the other profiles in Figure 3 probably due to poor resolution in the experimental measurements and in the computational grids [7].

Figure 4 presents the distribution of turbulence intensity u' normalized by the shear velocity at the bottom. Overall, the agreement between the numerical prediction by the RSM and the

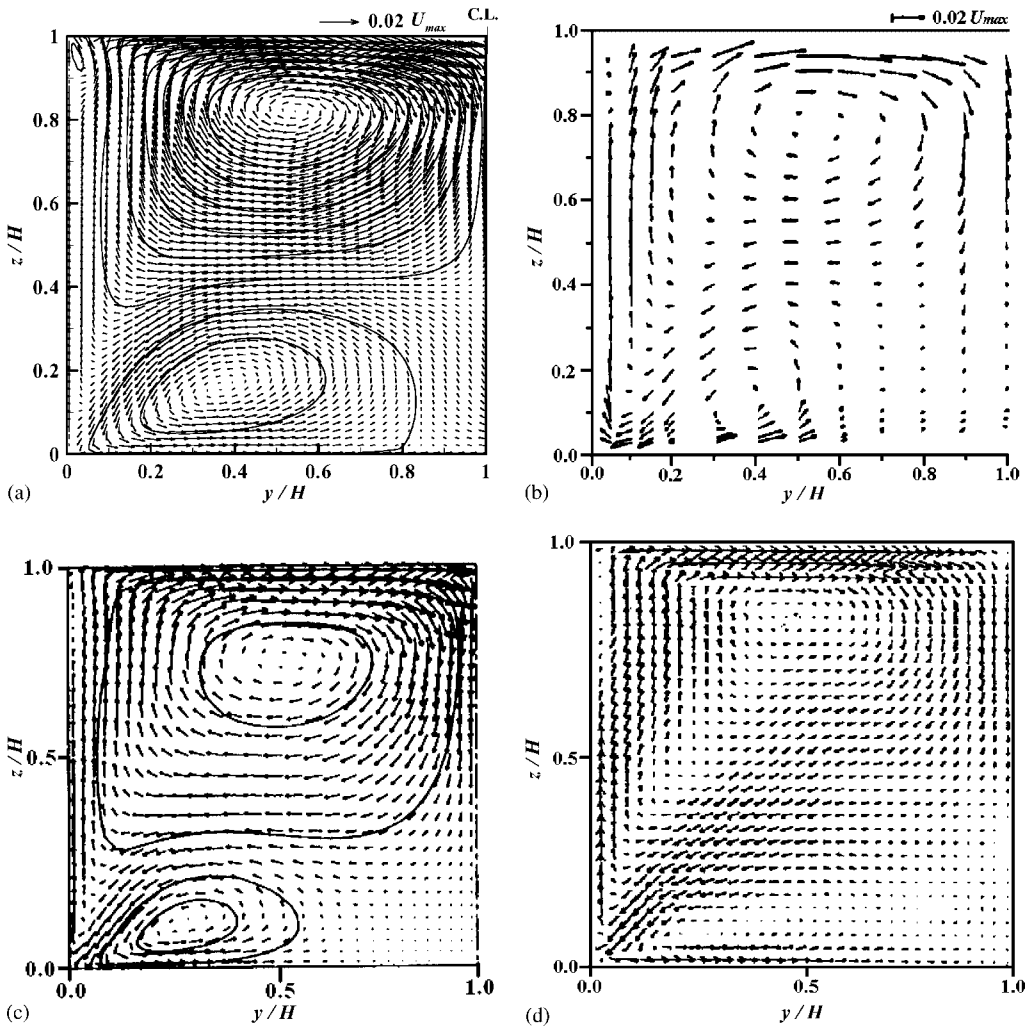

Figure 3. Secondary current vectors: (a) present RSM; (b) experiment [1]; (c) RSM [35]; and (d) LES [39].

measured profile by Nezu and Rodi [1] appears to be quite good. As stated before, the wall boundary and the free surface tend to reduce the turbulence intensity in the direction normal to the boundary, and the decreased amount of turbulence intensity is redistributed to those in directions parallel to the boundary, i.e. in both longitudinal and transverse directions. This redistribution of turbulence intensity increases the level of anisotropy in the vicinity of the boundary. In Figure 4, it can be seen that the turbulence intensity u' increases along the boundaries, i.e. the free surface, sidewall, and bottom. This is a direct effect of the redistribution of turbulence intensity. Note also that the contour lines of the turbulence intensity u' are bulged towards the juncture of the bottom and sidewall and towards the juncture of

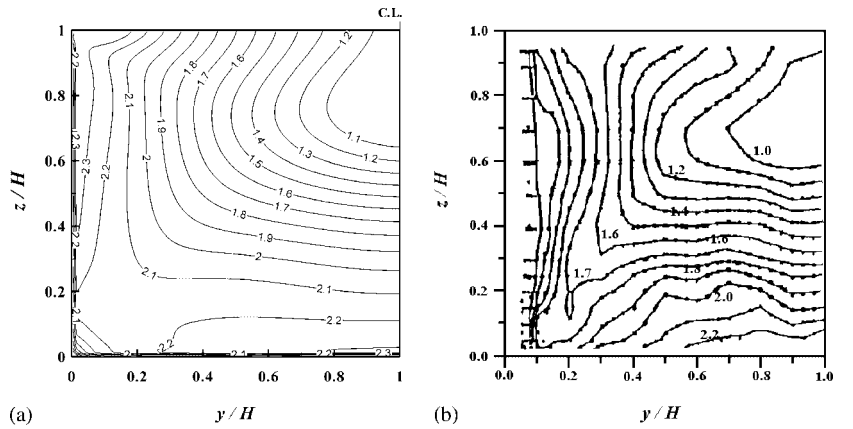

Figure 4. Turbulence intensity (u'/u_{*b}): (a) present RSM; and (b) experiment [1].

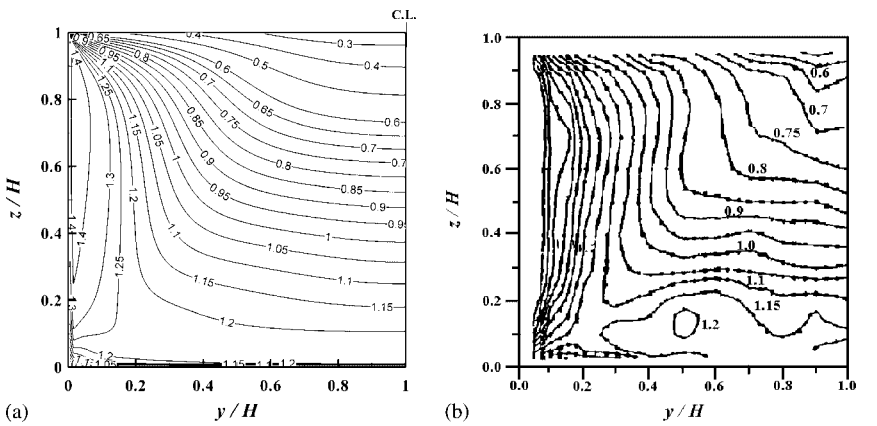

Figure 5. Turbulence intensity (w'/u_{*b}): (a) present RSM; and (b) experiment [1].

the free surface and sidewall, and the turbulence intensity u' increases towards each juncture. However, the bulge in the contour lines towards the upper juncture is not clearly observed in Figure 4(b). In addition, it should be noted that the minimum for u' occurs below the water surface, which is related with the velocity dip associated with secondary currents.

Figure 5 gives the distribution of the turbulence intensity w' normalized by the shear velocity at the bottom. The computed turbulence intensity w' was compared with the measured data by Nezu and Rodi [1], and good agreement was found. In the figure, it can be seen that w' decreases towards the water surface, while it increases towards the sidewall. This is also due to the redistribution of turbulence intensity along the boundary. In both results, the contour lines of the turbulence intensity are seen to bulge towards the juncture of the bottom and sidewall.

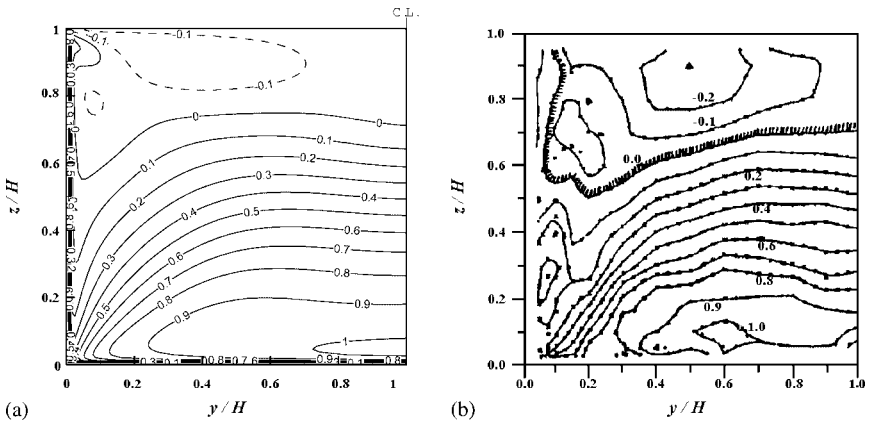

Figure 6. Reynolds stress ($-\overline{u'w'}/u_{*_b}^2$): (a) present RSM; and (b) experiment [1].

The distribution of Reynolds stress ($-\overline{u'w'}$) normalized by the squared shear velocity at the bottom is given in Figure 6. In this figure, the Reynolds stress profile simulated by the RSM compares favourably with the measured distribution. A general tendency observed is that the Reynolds stress increases as it approaches the bottom. It should also be noted in the figure that the Reynolds stress increases with the distance from the sidewall for $y/H < 0.6$. For $z/H > 0.7$, the Reynolds stress is negative, which is due to a velocity dip caused by secondary currents.

Figure 7 shows the distribution of shear stress at the sidewall, which is normalized by its mean value. For comparisons, both measured data by Nezu and Rodi [1] and various simulated data sets are given in the figure. All profiles in the figure indicate that the shear stress at the sidewall increases rapidly in the region close to the bottom, and becomes nearly uniform for $0.1 \leqslant z/H \leqslant 0.9$. However, the wall shear stress, as computed by the present RSM and LES data by Broglia *et al.* [42], shows a rapid increase for $z/H > 0.9$. The shear stress at the free surface appears to be about 60% higher than the mean value in the middle region. This is caused by inner secondary currents occurring at the juncture of the free surface and sidewall. That is, the inner secondary currents transfer high momentum from the centre to the sidewall near the free surface. Grega *et al.* [6] and Broglia *et al.* [42] confirmed this through laboratory experiments and LES. However, this phenomenon is not seen in the shear stress distributions at the sidewall by Cokljat [35], Shi *et al.* [39], and by Nezu and Rodi [1].

MECHANISM OF GENERATION OF SECONDARY CURRENTS

In order to investigate the mechanism by which secondary currents are generated in an open-channel flow, the following streamwise vorticity equation is considered:

$$\bar{v}\frac{\partial \Omega}{\partial y} + \bar{w}\frac{\partial \Omega}{\partial z} = \frac{\partial^2}{\partial y \partial z}\left(\overline{w'^2} - \overline{v'^2}\right) + \left(\frac{\partial^2}{\partial y^2} - \frac{\partial^2}{\partial z^2}\right)\overline{v'w'} + \nu\nabla^2\Omega \tag{13}$$

where Ω is the streamwise vorticity ($= \partial\bar{v}/\partial z - \partial\bar{w}/\partial y$). In Equation (13), the terms on the left-hand side represent the convection of the vorticity, and the first term on the right-hand side

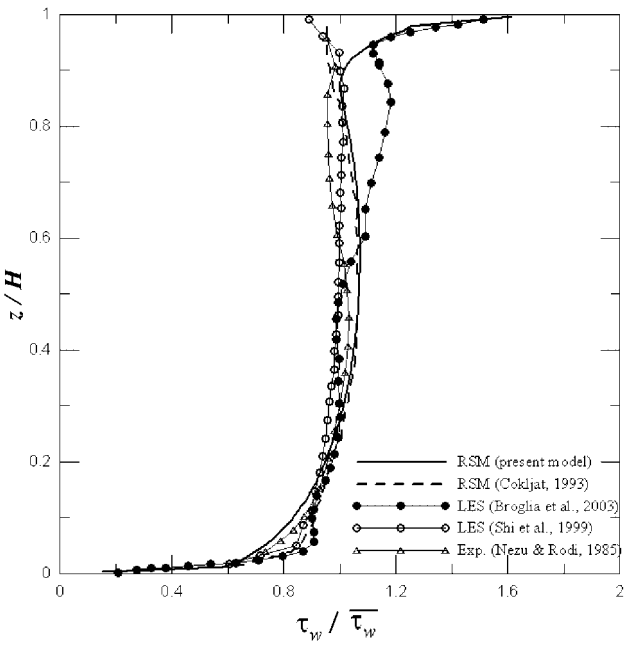

Figure 7. Sidewall shear stress distribution.

is the production by the anisotropy of Reynolds normal stress, the second term is production by Reynolds shear stress, and the third term is viscous diffusion.

Previous studies have revealed that both production terms by anisotropy of Reynolds normal stress and by Reynolds shear stress are larger in magnitude compared with the other terms in the vorticity transport equation, Equation (13). For example, Gessner and Jones [43] found that both production terms contribute to generating secondary currents in a square duct flow. Later, Nezu and Nakagawa [44] confirmed this through experiments of open-channel flows over sand ribbons, and Demuran and Rodi [23] reached the same conclusion through the numerical simulations of duct flows using the ASM. More specifically, Gessner [45] and Ohmoto and Hayashi [46] concluded that production by Reynolds shear stress is most responsible for the generation of secondary currents.

Figure 8 shows the distribution of the streamwise vorticity in the transverse plane. In the figure, the red region with solid contour lines and the blue region with dashed contour lines denote positive and negative vorticities, respectively. It can be seen in the figure that the vorticity is positive in most of the free surface region, representing the free surface vortex. Two negative vorticies are also observed in the left corners close to the bottom and to the free surface. The former denotes the bottom vortex, and the latter is formed due to inner secondary currents.

In order to investigate the mechanism of the generation of secondary currents, a budget analysis of the streamwise vorticity (Ω) was performed and the results are plotted in Figures 9 and 10. The figures show that the magnitude of production by anisotropy of Reynolds normal stress is about the same as that of production by Reynolds shear stress but their signs are

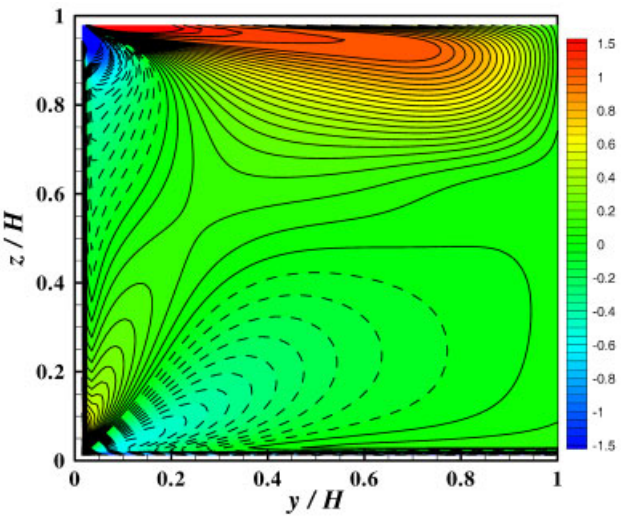

Figure 8. Distribution of streamwise vorticity (unit: s^{-1}).

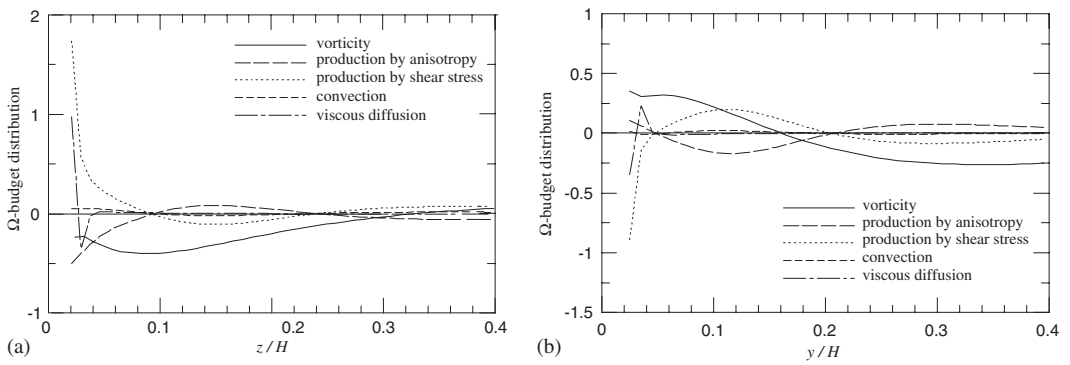

Figure 9. Generation of bottom vorticity: (a) $y/H = 0.25$; and (b) $z/H = 0.2$.

opposite. The two production terms appear to be much greater than convection term and viscous diffusion term everywhere except for the regions close to walls and free surface. This indicates that the balance between two production terms is responsible for generating the secondary currents.

Figures 9(a) and (b) show the Ω budget distributions along the vertical line at $y/H = 0.25$ and along the horizontal line at $z/H = 0.2$, respectively. In the figures, vorticity Ω is plotted with each term in the vorticity transport equation to show its sign. In Figure 9(a), both convection and viscous diffusion terms are seen to be extremely small except for the region close to the bottom. The vorticity is observed to be negative for $z/H < 0.32$. Specifically, for $z/H < 0.09$, it can be seen that production by anisotropy of Reynolds normal stress is

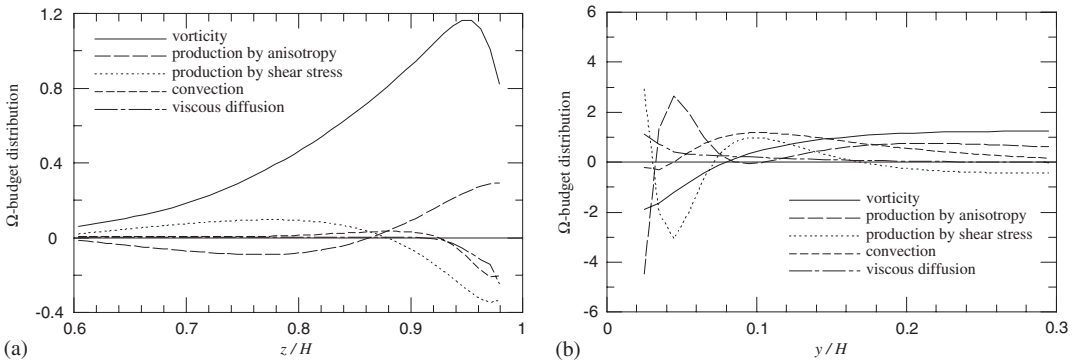

Figure 10. Generation of free surface vorticity: (a) $y/H = 0.5$; and (b) $z/H = 0.95$.

negative and production by Reynolds shear stress is positive. The situation is the opposite for $z/H > 0.09$. In addition, in Figure 9(b), it is observed that production by anisotropy of Reynolds normal stress has the same sign as vorticity for $y/H < 0.05$ and production by Reynolds shear stress has the same sign as the vorticity for $y/H > 0.21$. The foregoing results indicate that both production terms by anisotropy of Reynolds normal stress and by Reynolds shear stress play significant roles in generating bottom secondary currents. The production by anisotropy of Reynolds normal stress is important in the vicinity of the wall and production by Reynolds shear stress is important in more distant regions from the wall. This is consistent with the findings by DNS of square duct flows by Huser and Biringen [47].

For the free surface vortex, a similar analysis was carried out. Figures 10(a) and (b) present the Ω budget distributions along the vertical line at $y/H = 0.5$ and along the horizontal line at $z/H = 0.95$, respectively. In Figure 10(a), a positive vorticity is observed for $0.6 < z/H < 1.0$. Specifically, it appears that productions by Reynolds shear stress and by the anisotropy of Reynolds normal stress play key roles in generating secondary currents for $z/H < 0.85$ and for $z/H > 0.85$, respectively. It is also interesting to note in the figure that the convection term is not zero while viscous diffusion is negligible except for the region close to the water surface. This suggests that the convection term contributes to generating the free surface vortex unlike the case of the bottom vortex. Also, for the duct flow or the channel flow without free surface, previous studies of the Ω-budget analysis reported the same result that both production terms are dominant over the entire domain except for the wall region [43, 47–50]. In Figure 10(b), a positive vortex and a negative vortex are observed for $y/H > 0.08$ and for $y/H < 0.08$, indicating the outer and the inner secondary currents, respectively. For inner secondary currents, production by anisotropy of Reynolds normal stress is important in the region close to the sidewall, i.e. for $y/H < 0.035$, and production by Reynolds shear stress is important in the region more distant from the sidewall, i.e. for $0.035 < y/H < 0.07$. For the outer secondary currents, production by anisotropy of Reynolds normal stress and the convection term contribute to generating a vortex for $y/H > 0.17$. In the transition region where vorticity changes its direction from inner to outer secondary currents, i.e. for $0.07 < y/H < 0.17$, production by Reynolds shear stress, convection, and production by anisotropy of Reynolds normal stress contribute to generating the secondary currents.

CONCLUSIONS

A Reynolds stress model is presented for the numerical simulation of fully developed turbulent flows in an open-channel. The Reynolds stress model is composed of Speziale *et al.*'s model for the pressure–strain term and Mellor and Herring's model and Rotta's model for diffusion and dissipation of Reynolds stress, respectively. The computed mean flow and turbulence characteristics were compared with the results of simulations as well as with previously-reported experimental data. Comparisons revealed that the developed Reynolds stress model successfully predicts the mean and turbulent features of open-channel flows. Moreover, the model reproduced the inner secondary currents at the juncture of the sidewall and free surface. The inner secondary currents were also shown to significantly increase the wall shear stress near the free surface.

The mechanism by which secondary currents are generated was investigated by performing a budget analysis of the streamwise vorticity. The findings showed that both production terms by anisotropy of Reynolds normal stress and by Reynolds shear stress contribute to the generation of bottom secondary currents. Specifically, the production by the anisotropy of Reynolds normal stress plays a key role in the vicinity of the wall and production by Reynolds shear stress is important in the region more distant from the wall. For the free surface vorticity, the generating mechanisms of both outer and inner secondary currents could be explained through the analysis. For outer secondary currents, production by anisotropy of Reynolds normal stress and production by Reynolds shear stress are important in the generation of secondary currents in regions close to the free surface and away from the free surface, respectively. This is a common feature which can be applied to the generation of the inner secondary currents. However, the convection term was shown to play an important role in the generation of outer secondary currents unlike the case of the bottom secondary current.

ACKNOWLEDGEMENTS

This study was supported by the 2003 Core Construction Technology Development Project (03-SANHAKYOUN-C03-01) through the Urban Flood Disaster Management Research Center in KICTTEP of MOCT KOREA.

REFERENCES

1. Nezu I, Rodi W. Experimental study on secondary currents in open channel flow. *21st IAHR Congress*, Melbourne, Australia, 1985; **2**:19–23.
2. Matthes GH. Macroturbulence in natural stream flow. *Transactions* (AGU) 1947; **28**:255–265.
3. Nikuradse J. Turbulente stromung im inner des rechteckigen offenen kanals. *Forschungsarbeiten* (Heft) 1926; **281**:36–44.
4. Gosh S, Roy N. Boundary shear distribution in open channel flow. *Journal of the Hydraulic Division* (ASCE) 1970; **96**(HY4):967–994.
5. Naot D, Rodi W. Calculation of secondary currents in channel flows. *Journal of the Hydraulic Division* (ASCE) 1982; **108**(HY8):948–968.
6. Grega LM, Wei T, Leighton RI, Nevens JC. Turbulent mixed boundary flow in a corner formed by a solid wall and a free surface. *Journal of Fluid Mechanics* 1995; **294**:17–46.
7. Hsu TY, Grega LM, Leighton RI, Wei T. Turbulent kinetic energy transport in a corner formed by a solid wall and a free surface. *Journal of Fluid Mechanics* 2000; **410**:343–366.
8. Sundermann J, Puls W. Numerical model of sediment transport in coastal waters. *Mathematical Modeling of Estuarine Physics*, vol. 1. Springer: New York, 1980; 253–265.
9. Peric M, Ruger M, Scheuerer G. Calculation of the two dimensional turbulent flow over a sand dune model. *Report No. SRR-TN-88-02*, University of Erlangen, Germany, 1988.

10. Cheong HF, Xue H. Turbulence model for water flow over two-dimensional bed forms. *Journal of Hydraulic Engineering* (ASCE) 1997; **123**(5):402–409.
11. Bravo HR, Zheng YH. Turbulent flow over step with rounded edges: experimental and numerical study. *Journal of Hydraulic Engineering* (ASCE) 2000; **126**(1):82–85.
12. Fischer-Antze T, Stoesser T, Bates P, Olsen NRB. 3D numerical modeling of open channel flow with submerged vegetation. *Journal of Hydraulic Engineering* (IAHR) 2000; **39**(3):303–310.
13. Wu W, Rodi W, Wenka T. 3D numerical modeling of flow and sediment transport in open channels. *Journal of Hydraulic Engineering* (ASCE) 2000; **126**(1):4–15.
14. Rameshwaran P, Naden PS. Three dimensional numerical simulation of compound channel flows. *Journal of Hydraulic Engineering* (ASCE) 2003; **129**(8):645–652.
15. Pezzinga G. Velocity distribution in compound channel flows by numerical modeling. *Journal of Hydraulic Engineering* (ASCE) 1994; **120**(10):1176–1198.
16. Cokljat D, Younis BA. Second-order closure study of open channel flows. *Journal of Hydraulic Engineering* (ASCE) 1995; **121**(2):94–107.
17. Bernard PS, Wallace JM. *Turbulent Flow Analysis*, *Measurement*, *and Prediction*. Wiley Inc.: Hoboken, NJ, 2002.
18. Lin B, Shiono K. Numerical modeling of solute transport in compound channel flows. *Journal of Hydraulic Research* (IAHR) 1995; **33**(6):773–788.
19. Sofialidis D, Prinos P. Compound open-channel flow modeling with nonlinear low-Reynolds k–ε models. *Journal of Hydraulic Engineering* (ASCE) 1998; **124**(3):253–262.
20. Krishnappan BG, Lau YL. Turbulence modeling of flood plain flows. *Journal of Hydraulic Engineering* (ASCE) 1986; **112**(4):251–266.
21. Naot D, Nezu I, Nakagawa H. Hydrodynamic behavior of compound rectangular open channels. *Journal of Hydraulic Engineering* (ASCE) 1993; **119**(3):390–408.
22. Naot D, Nezu I, Nakagawa H. Hydrodynamic behavior of partly vegetated open channels. *Journal of Hydraulic Engineering* (ASCE) 1996; **122**(11):625–633.
23. Demuran AO, Rodi W. Calculation of turbulence driven secondary motion on non circular ducts. *Journal of Fluid Mechanics* 1984; **140**:189–222.
24. Reece GJ. A generalized Reynolds stress model of turbulence. *Ph.D. Thesis*, Imperial College, University of London, London, England, 1977.
25. Launder BE, Reece GJ, Rodi W. Progress in the development of Reynolds stress turbulence closure. *Journal of Fluid Mechanics* 1975; **63**(3):537–566.
26. Cokljat D, Younis BA. Compound-channel flows: a parametric study using a Reynolds stress transport closure. *Journal of Hydraulic Research* (IAHR) 1995; **121**(2):94–107.
27. Basara B, Cokljat D. Reynolds stress modeling of turbulent flows in meandering open-channels. *Industrial and Environmental Applications of Fluid Mechanics* (ASME) 1995; **221**:27–32.
28. Speziale CG, Sarkar S, Gatski T. Modeling the pressure strain correlation of turbulence: an invariant dynamical systems approach. *Journal of Fluid Mechanics* 1991; **227**:245–272.
29. Mellor GL, Herring HJ. A survey of mean turbulent field closure. *AIAA Journal* 1973; **11**:590–599.
30. Rotta JC. Statistische theorie nichthomogener turbulenz. *Zeitschrift fur Physik* 1951; **129**:547–572.
31. Choi S-U, Kang H. Numerical tests of Reynolds stress closure models in the computations of open-channel flows. *The 8th International Symposium on Flow Modeling and Turbulence Measurements*, Tokyo, Japan, 2001.
32. Demuren AO, Sarkar S. Perspective: systematic study of Reynolds stress closure models in the computations of plane channel flows. *Journal of fluids Engineering* (ASME) 1993; **115**:5–12.
33. Shir CC. A preliminary study of atmospheric turbulent flow in the idealized planetary boundary layer. *Journal of Atmospheric Science* 1973; **30**:1327–1339.
34. Gibson MM, Launder BE. Ground effects on pressure fluctuations in the atmospheric boundary layer. *Journal of Fluid Mechanics* 1978; **86**:491–511.
35. Cokljat D. Turbulence models for non-circular ducts and channels. *Ph.D. Thesis*, Department of Civil Engineering, City University, London, England, 1993.
36. Patankar SV, Spalding DB. A calculation procedure for heat, mass and momentum transfer in three dimensional parabolic flows. *International Journal of Heat and Mass Transfer* 1972; **15**(10):1787–1806.
37. Patankar SV. *Numerical Heat Transfer and Fluid Flow*. Hemisphere Publishing Corporation/Taylor & Francis Group: New York, 1980.
38. Kang H. Reynolds stress modeling of vegetated open-channel flows. *Ph.D. Thesis*, School of Civil and Environmental Engineering, Yonsei University, Seoul, Korea, 2005.
39. Shi J, Thomas TG, Williams JJR. Large eddy simulation of flow in a rectangular open channel. *Journal of Hydraulic Research* (IAHR) 1999; **37**(3):345–361.
40. Daly BJ, Harlow FH. Transport equations in turbulence. *Physics of Fluids* 1970; **13**:2634–2649.
41. Tominaga A, Ezaki K, Nakagawa H. Three dimensional turbulent structure in straight open channel flows. *Journal of Hydraulic Research* (IAHR) 1989; **27**(1):149–173.

42. Broglia R, Pascarelli A, Piomelli U. Large eddy simulations of ducts with a free surface. *Journal of Fluid Mechanics* 2003; **484**:223–253.
43. Gessner BF, Jones JB. On some aspects of fully developed turbulent flow in rectangular channels. *Journal of Fluid Mechanics* 1965; **23**:689.
44. Nezu I, Nakagawa H. Cellular secondary currents in straight conduit. *Journal of Hydraulic Engineering* (ASCE) 1984; **110**(2):173–193.
45. Gessner FB. The origin of secondary flow in turbulent flow along a corner. *Journal of Fluid Mechanics* 1973; **58**:1–25.
46. Ohmoto T, Hayashi S. Study of generation mechanism of secondary currents in open-channel flow by direct numerical simulation. *Journal of Hydroscience and Hydraulic Engineering* 2003; **21**(1):11–21.
47. Huser A, Biringen S. Direct numerical simulation of turbulent flow in a square duct. *Journal of Fluid Mechanics* 1993; **257**:65–95.
48. Perkins HJ. The formation of streamwise vorticity in turbulent flow. *Journal of Fluid Mechanics* 1970; **44**:721–740.
49. Madabhushi RK, Vanka SP. Large eddy simulation of turbulence-driven secondary flow in a square duct. *Physics of Fluids* 1991; **3**(11):2734–2745.
50. Gavrilakis S. Numerical simulation of low-Reynolds number turbulent flow through a straight square duct. *Journal of Fluid Mechanics* 1992; **244**:101–129.

